Real-time Location-based Utilization of IRSs for mmWave Sensing in Multiuser 6G Networks

Alejandro Amat*, Filip Lemic*§, Jalal Jalali†, Xavier Costa Perez*¶‖

*AI-Driven Systems Lab, i2Cat Foundation, Spain
†Internet and Data Lab, University of Antwerp - imec, Belgium
¶NEC Laboratories Europe GmbH, Germany
‖ICREA, Spain
Email: filip.lemic@i2cat.net

Abstract—

I. INTRODUCTION

Virtual Reality (VR)) is continuously transforming our digital interactions, offering innovative solutions in various domains such as healthcare, tourism, education, entertainment, and occupational safety [1]. The advancement of VR hardware and content is progressing rapidly, with a primary focus on elevating the immersiveness of VR experiences by enhancing the quality of video content presented to users and striving to eliminate the need for physical connections by enabling seamless wireless delivery of video content [2] . Another crucial objective is to enable collaborative multiuser experiences, where users can interact and cooperate within the virtual realm, and the actions of one user become virtual content that impacts the experiences of other, possibly colocated users [3].

In the foreseeable future, VR systems are poised to accommodate multiple fully-immersed users who can freely navigate their Virtual Experiences (VEs). To enable such setups, advanced wireless communication networks will be essential, primarily operating in the millimeter Wave (mmWave) frequency band, spanning from 30 to 300 GHz. These networks must offer highly directional transmission and reception capabilities to ensure seamless real-time delivery of high-quality video content to mobile VR users [4]. These directional mmWave beams are also expected to continuously track users' movements to maintain Line-of-Sight (LoS) connectivity, thus optimizing video quality. Simultaneously, the concept of Machine Learning (ML)-based redirected walking is being explored to prevent collisions among co-located users and between users and the boundaries of confined VR environments [3]. This approach allows VR users to move freely within the virtual realms while discreetly guiding them within the physical setups to avoid collisions, enhancing the overall immersion in the VEs.

The interactive multi-user VE envision truthfully reproducing the actions of one user in the VEs of the other, potentially collocated users. Such interaction should be reproduced within the motion-to-photon latency of less than 20 ms to avoid causing nausea to the users [5]. Such motion capturing is traditionally performed using cameras strategically positioned in the environment [6]. However, such approaches by-design do not guarantee privacy preservation and induce significant delays due to cross-layer information collection and image processing overheads. More recently, high-frequency Integrated Communication and Sensing (ISAC) approaches have gained traction, in which the same communication wavefront is envisioned to be utilized for both tracking of the users and high throughput communication with them [7]. At the same time, passive sensing in the form of mmWave radar is envisaged to be employed for more advanced sensing tasks such as motion recognition or 3-Dimensional (3D) pose estimation [8].

In full-immersive VR applications, maintaining stable throughput is of prime importance for maintaining the users' Quality of Service (QoS) throughout their VEs. At the same time, active ISAC sensing tasks require the maximization of the Signal-to-Noise Ratio (SNR) of the communication wavefront for accuracy maximization [7]. These challenging requirements cannot be achieved with existing mmWave hardware such as IEEE 802.11ad/ay Access Points (APs), primarily due to the low number of antenna elements in the practical realization of mmWave transceivers, causing unequal coverage in the deployment environment, as will be demonstrated in the paper. An additional challenge comes from the fact that LoS communication with the users might be interrupted due to the presence of multiple users in the deployment environment, causing significant throughput and SNR degradation.

To counter these challenge, we introduce Intelligent Reflective Surfaces (IRSs) to the considered full-immersive multiuser VR environments. Given that such environments will have to be safe spaces without collision hazards for the users apart from the environmental boundaries and other users [3], we consider it as a natural possibility to utilize IRSs in the surrounding walls to support the communication and sensing challenges stemming from the scenario. IRSs consist of large arrays of passive reflecting elements on a reconfigurable planar surface. These elements can independently modify the phase of an incoming signal before reflecting it towards its intended receiver. The integration of IRS can be a boon for users experiencing significant path loss, as the IRS creates additional propagation pathways – namely, reflected channels. Moreover, these IRSs offer added degrees of freedom through the phase shifts of the reflective elements, which can be harnessed to
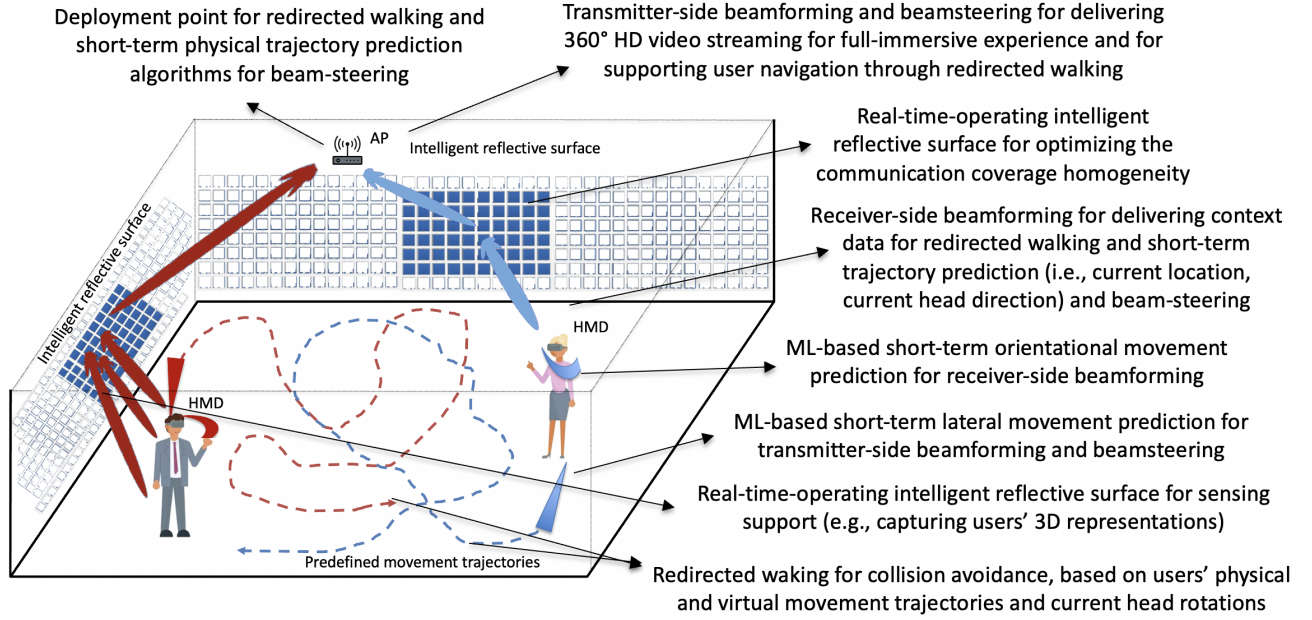
Figure 1: Considered scenario

minimize interference [8]. It is also worth noting that IRSs are envisioned to be manufactures as passive, cheap, and flexible entities adaptable for indoor VR streaming setups, as they could be used as "soft" environmental boundaries [9].

For the full-immersive VR scenario in Figure 1, we study a novel IRS location optimization, where a multi-antenna AP transmits information symbols to a set of single-antenna Head Mounted Devices (HMDs).

Notations: Boldface lower-case and upper-case letters represent vectors and matrices, respectively, e.g., $\mathbf{x}$ for vectors and $\mathbf{X}$ for matrices. The operators $(\cdot)^*$, $(\cdot)^T$, and $(\cdot)^H$ signify the conjugate, the transpose, and the conjugate transpose of a matrix or vector, respectively. The functions $\text{tr}(\cdot)$, $\text{vec}(\cdot)$, and $\text{diag}(\cdot)$ refer to the trace, vectorization, and diagonalization of a matrix, respectively. The notation $[\cdot]_{i,j}$ represents the (i,j)-th entry of a matrix. The symbol j is defined as $\sqrt{-1}$. The functions $\Re(\cdot)$ and $\arg(\cdot)$ denote the real part and the phase of a complex value, respectively. The symbols $\otimes$ and $\odot$ signify the Kronecker and Hadamard products between matrices or vectors, respectively.

II. SYSTEM OVERVIEW

We consider a scenario as depicted in Figure 1. Specifically, we consider an environment in which the users are immersed in their VEs. The environment is constrained in its physical size as to provide a safe space for the users to immerse in their experiences. As such, the only potential collision perils for the users are other users and environmental boundaries. Redirected Walking (RDW) is employed for directing the users primarily in a way that does not break their immersion, as discussed in Section ??. The users are immersed in VEs that are potentially unbound and interactive in the way that the action of one user affects the experience of the other, potentially collocated users. The perception of unbounded experiences are supported

through RDW by introducing imperceivable rotational, translational, and curvature gains, as discussed previously.

In such a scenario, the goal is to provide the users with the consistently high throughput throughout their VEs. As such, the communication throughput between the AP and the users' HMD should be maximized, while simultaneously providing homogeneous coverage or minimizing the spatial variability of the throughput. This is of interest as it allows for downlink transmission of the video content toward the users' HMDs in a way that minimizes the jitter and allows for continuous delivery of same-quality video frames. The fact that the users' VEs might be interactive poses an additional system requirement. Specifically, there is a need for capturing the actions of the users, as well as delivering the captured content to other users, where both actions should be carried out within the motion-to-photon latency for immersion maximization and avoiding the motion sickness.

To support the outlined scenario's requirements, we envision the utilization of high-frequency wireless networks operating in mmWave frequencies (i.e., 30-300 GHz). This is because the delivery of VR content in real time, as well as real time sensing and distribution of users' actions across other users, requires significant communication bandwidth not present in traditional sub-6 GHz frequencies. In addition, large communication bandwidth available at such frequencies represents a primer for accurate network-supported sensing of users' actions, e.g., in the form of digital capturing of users full 3D poses.

Due to all these needs for our scenario, we have used IEEE 802.11ad networks. The IEEE 802.11ad standard operates at mmWave frequencies, which makes directional communication a feature to allow high speeds over short distances. This is achieved through advanced beamforming techniques, in which the AP and user equipments (UEs) can focus their transmissions in specific directions, improving signal strength and

reliability. However, this directional nature of communication can create challenges in achieving uniform coverage within a given area [10]. The quality in the formation of beams varies with the number of antennas; as the number of antennas increases, the width of the beam is reduced, making the array more directional, thus improving beamforming. At the same time, as the number of antennas decreases, the beamforming declines [11]. When the number of antenna elements in a AP is limited, achieving uniform coverage over the entire area becomes difficult. This limitation can result in areas of weaker signal strength or coverage gaps, which can be particularly problematic for applications such as VR.

IRS has recently been proposed as a cost-effective solution for achieving high spectrum and energy efficiency low-cost reflecting elements. An IRS is composed of many passive elements, each able to reflect the incident signal with an adjustable phase shift, thus significantly enhancing the communication performance without needing to deploy additional active Base Stations (BSs) or relays. Moreover, from the implementation perspective, IRS possess appealing features such as low profile and lightweight, thus, can be easily mounted on walls [12].

Therefore, we have considered covering the walls of the room, as illustrated in Figure 1 of our proposal. The fundamental premise is that communication performance can be improved in real-time. Each instance of user movement initiates a computation to determine the optimal IRSs' placement where s' is the coordinate of the centre position of the IRS . As the IRS covers the room wall, the algorithm will calculate the optimal IRSs' placement where the beam will be directed improving communication quality. The need for quick and real-time calculations explained in Section **??** that take into account the UEs precise location within the room and the relative position of the AP within the VR environment is integral to this dynamic framework. It is required to avoid excessive engineering due to the time-sensitive nature of the operation.

Accordingly, looking at Figure 1, the points that are study with in this work will be real-time-operating IRS for optimizing the communication coverage homogeneity and real-time-operating IRS for sensing support (e.g., capturing users' 3D representations)

III. REAL-TIME LOCATION-BASED UTILIZATION OF IRSS FOR MMWAVE SENSING

In many real-world applications, the utilization of IRS for wireless communication proves to be advantageous. For instance, employing IRS sequentially communicate with UE can be a cost-effective choice in scenarios where delays cannot be tolerated, such as periodic sensing data collection, as is the case in high data-rate Virtual Reality (VR) networks. As illustrated in Fig. 1, we investigate a wireless communication system in which IRSs are employed to redirect data to a set of UEs. The collection of all UEs is denoted as $\mathcal{K} = 1, ..., K$, while the set of IRSs is represented as $\mathcal{I} = 1, ..., I$, with each element of an IRS being denoted by $\mathcal{M} = 1, ..., M$. Our

objective is to optimize the position of the IRSs to maximize the Signal-to-Noise Ratio (SNR) over a fixed time duration $T > 0$. Sustaining a high SNR is of paramount importance to ensure extensive and dependable coverage, leading to stronger signals, minimized dead zones, and enhanced comprehensive data collection, ultimately improving communication and sensing capabilities. The time duration T is divided into N evenly spaced time intervals, defined as $T = N\xi_t$. More precisely, ξ_t signifies the duration of each individual time slot, and N represents the set of all these time slots, denoted as $\mathcal{N} = 1, ..., N$.

In this context, we utilize a 3D Cartesian coordinate system to track the positions of the AP, UEs, and IRSs. The AP is fixed at coordinates $\boldsymbol{a} = [a_x, a_y, a_z]^T \in \mathbb{R}^{3 \times 1}$. On the other hand, the UEs are randomly scattered in a vertical plane, and their predefined trajectory follows the path $\boldsymbol{u}[n, k] = [u_x[n, k], u_y[n, k], u_z[n, k]]^T \in \mathbb{R}^{3 \times 1}$. The placement of the IRSs' is pivotal for signal redirection. When projected onto the vertical plane (e.g., on each wall of a room or office enforcement), the central location of i-th IRS is represented by $\boldsymbol{s}^i[n] = [s_x^i[n], s_y^i[n], s_z^i[n]]^T \in \mathbb{R}^{3 \times 1}$. Furthermore, we confine the area of interest to $\mathcal{I}$ half-have spaces $\mathcal{D}_\infty = \{\mathcal{D}_1, ..., \mathcal{D}_I\}$ where each IRSs' could potentially be placed[1]. Within the first half-space, the first IRS can be strategically positioned, and as such, we define $\mathcal{D}_1$ as:

$$
\begin{aligned}
y_{min} < &s_y^i[n] < y_{max}, , \\
z_{min} < &s_z^i[n] < z_{max}, \\
&s_x^i[n] = \{x_{min}, x_{max}\}, \ \forall n \in \mathcal{N}, \forall i \in \mathcal{I}, \quad (1)
\end{aligned}
$$

$$
\begin{aligned}
x_{min} < &s_x^i[n] < x_{max}, \\
z_{min} < &s_z^i[n] < z_{max}, \\
&s_y^i[n] = \{y_{min}, y_{max}\}, \ \forall n \in \mathcal{N}, \forall i \in \mathcal{I}. \quad (2)
\end{aligned}
$$

The equations in (1) and (2) define the first half-space region, i.e., $\mathcal{D}_1$, where the first IRS needs to be centrally positioned. Likewise, we can establish $\mathcal{D}_\infty / \mathcal{D}_1 = \{\mathcal{D}_2, ..., \mathcal{D}_I\}$ to represent the regions within which the remaining IRSs are positioned. These regions make sure that IRSs' are positioned in one of the corner walls of the room as depicted in Fig. 1.

In this configuration, the distance between the IRS and the UE, as well as between the IRS and the AP, evolves over time and significantly impacts the quality of the communication channel. Therefore, determining the optimal placement of the IRS is of utmost importance. To provide clarity to our discussion, we make the assumption that the communication link between the IRS and the UE is predominantly governed by the Line of Sight (LoS) channel. It is noteworthy that, within our setup, the IRS-UE channel is more likely to maintain a strong LoS link compared to the AP-UE channels. We make this assumption while considering that the AP-UE channel is

[1]We strategically place each IRS central position in any of these half-space regions to optimize signal quality, minimize interference, and enhance overall wireless communication system efficiency. This is done so long as no two IRS are placed in one half-space; that is, each IRS must be positioned in a different half-space.

entirely obstructed by other UEs, which block the Line of Sight between the AP and the UE. We reserve the exploration of Non-Line of Sight (NLoS) and multi-path fading channels for our future studies. Additionally, we presume that any Doppler effect induced by UE mobility is fully compensated for in our analysis. To expedite the utilization of an IRS-aided communication, we also take into account the radiation pattern of the IRS, as explored in [13], namely:

$$F(\psi_{i,k}, \varphi_i) = \begin{cases} \cos^3(\psi_{i,k}), & \psi_{i,k} \in [0, \pi/2], \varphi_i \in [0, 2\pi], \\ 0, & \psi_{i,k} \in (\pi/2, \pi], \varphi_i \in [0, 2\pi], \end{cases}$$
(3)

where $\psi_{i,k}$ and φ_i represent the elevation and azimuth angles, respectively, from each IRS to the AP/UE link. It is important to note that the radiation pattern of the IRS remains consistent across various azimuth angles. To simplify our discussion, we omit the argument φ_i from the function $F(\psi_{i,k}, \varphi_i)$ in (3) in subsequent equations, using $F(\psi_{i,k})$ in place of $F(\psi_{i,k}, \varphi_i)$. Under these conditions, the dynamic channel between the AP and the IRS, as well as between the IRS and the k-th UE, follows the free-space path loss model, which can be described as:

$$\tilde{\mathbf{h}}_i = \mathbf{h}_i \sqrt{\beta_{i,0} F(\psi_{i,0})}, \tag{4}$$

$$\tilde{\mathbf{g}}_{i,k} = \mathbf{g}_{i,k} \sqrt{\beta_{i,k} F(\psi_{i,k})}, \forall k \in \mathcal{K}, \tag{5}$$

where $\beta_{i,0}$ and $\beta_{i,k}$ serve to quantify path loss, representing the reduction in signal strength as it traverses the wireless medium. In contrast, the vectors $\mathbf{h}_i \in \mathbb{C}^{M \times 1}$ and $\mathbf{g}_{i,k} \in \mathbb{C}^{M \times 1}$ describe small-scale fading, accounting for the rapid signal fluctuations attributed to phenomena like multipath propagation and signal scattering. Notably, these small-scale fading characteristics exhibit relative stability throughout each coherence interval, allowing us to treat them as quasi-static. Meanwhile, path loss, influenced by distance and environmental obstructions, undergoes variations, albeit at a much slower pace. This perspective is rooted in the substantial difference in scales between the distances separating users, the AP, and the IRS and the distances between individual IRS elements, where variations occur much more swiftly and are, therefore, considered negligible in comparison, aligning with existing wireless communication literature [14], [15]. In light of this, the path loss components can be represented as:

$$\beta_{i,k'} = c_0 \| \mathbf{d}_{i,k'}[n] \|^{-\alpha_{i,k'}}, \forall k' \in \mathcal{K} \cup \{0\} \forall i \in \mathcal{I}, \forall n \in \mathcal{N}, \tag{6}$$

where c_0 is the reference path loss at a distance of 1 meter. $\alpha_{i,0}$ and $\alpha_{i,k}, \forall k \in \mathcal{K}$ are the path loss exponents of links between AP and IRS and the link between IRS and UE k, respectively [16], [17]. Moreover, the distance vectors from

the IRS to the AP and k-th UE are respectively given by:

$$\mathbf{d}_{i,0}[n] = \mathbf{s}^i[n] - \mathbf{a}[s_x^i[n] - a_x, s_y^i[n] - a_y, s_z^i[n] - a_z]^T,$$
$$\forall i \in \mathcal{I}, \forall n \in \mathcal{N}, \tag{7}$$

$$\mathbf{d}_{i,k}[n] = \mathbf{s}^i[n] - \mathbf{u}[n, k] = [s_x^i[n] - u_x[n, k], s_y^i[n] - u_y[n, k],$$
$$s_z^i[n] - u_z[n, k]]^T,$$
$$\forall k \in \mathcal{K}, \forall i \in \mathcal{I}, \forall n \in \mathcal{N}. \tag{8}$$

To sum it up, the mathematical representation for the received signal at the k-th UE is as follows:

$$y_k = \sum_{i \in \mathcal{I}} \sqrt{P_{\text{AP}}} \tilde{\mathbf{g}}_{i,k}^H \boldsymbol{\Theta}_i \tilde{\mathbf{h}}_i + n_k, \forall k \in \mathcal{K}. \tag{9}$$

where P_{AP} is the transmit power of the AP, and n_k corresponds to the additive white Gaussian noise (AWGN) observed at the k-th UE. The noise follows a complex normal distribution characterized by a mean of zero and a variance of σ_k^2. The i-th IRS phase shift matrix is represented by $\boldsymbol{\Theta}_i$ and is defined as $\boldsymbol{\Theta}_i \equiv \text{diag}(\theta_{1,m}, \theta_{2,m}, \ldots, \theta_{i,M})$. Here, $\theta_{i,m} \in \mathbb{C}$ characterizes the reflection coefficient associated with the m-th element of the i-th IRS. Specifically, $\theta_{i,m} \equiv \varrho_{i,m} e^{j\vartheta_{i,m}}$, where $\varrho_{i,m}$ lies within $[0, 1]$, capturing the reflection amplitude, and $\vartheta_{i,m}$ spanning $[0, 2\pi]$ depicts the phase shift of the m-th element of the i-th IRS. It is worth noting that the exponent 'j' in the equation represents the imaginary unit. In the absence of multi-user interference, we can express the SNR at the k-th UE as follows:

$$\gamma_{i,k}(P_{\text{AP}}, \boldsymbol{\Psi}_i, \boldsymbol{\beta}_i, \boldsymbol{\Theta}_i) = \frac{P_{\text{AP}} \beta_{i,0} F(\psi_{i,0}) \beta_{i,k} F(\psi_{i,k}) \left| \mathbf{g}_{i,k}^H \boldsymbol{\Theta}_i \mathbf{h}_i \right|^2}{\sigma_k^2},$$
$$\forall k \in \mathcal{K}, \forall i \in \mathcal{I}, \tag{10}$$

where $\boldsymbol{\Psi}_i$ and $\boldsymbol{\beta}_i$ encompass the sets of $\psi_{i,k}$'s and $\beta_{i,k}$'s, organized respectively as follows: $\boldsymbol{\Psi}_i \triangleq [\psi_{i,0}, ..., \psi_{i,K}]$ and $\boldsymbol{\beta}_i \triangleq [\beta i, 0, ..., \beta_{i,K}]$. These variables are instrumental in representing each IRS location decision variable in terms of $\boldsymbol{\beta}_i$. Given the SNR expression as articulated above, the optimization problem can be formulated as:

$$\max_{P_{AP}, \boldsymbol{\Psi}_i, \boldsymbol{\beta}_i, \boldsymbol{\Theta}_i} \gamma_{i,k}(P_{\text{AP}}, \boldsymbol{\Psi}_i, \boldsymbol{\beta}_i, \boldsymbol{\Theta}_i), \tag{11a}$$

$$\text{s.t. } P_{\text{AP}} \le P_{\text{AP}}^{\max}, \tag{11b}$$

$$|\theta_{i,m}| \le 1, \forall m \in \mathcal{M}, \forall i \in \mathcal{I}, \tag{11c}$$

$$\mathbf{s}^i[n] \in \mathcal{D}_i, \forall i \in \mathcal{I}, \forall n \in \mathcal{N}. \tag{11d}$$

Constraint (11b) guarantees that the transmission power of the AP remains within the specified upper limits. Constraint (11c) defines the operational boundaries for the reflection coefficients of each IRS element. Constraint (11d) enforces the placement of IRSs on one of the corner walls of the room. Due to the presence of a non-concave objective function and the non-convex nature of constraint (11c), the optimization problem outlined in (11) is inherently nonconvex. This complexity poses a challenge in finding an optimal solution to the problem. Consequently, addressing non-convexity may require

the use of optimization techniques or approximations, such as Alternating Optimization (AO) methods, to effectively tackle the problem.

A. AP Transmit Power Control

To start, we hold $\boldsymbol{\Psi}_i$, $\boldsymbol{\beta}_i$, and $\boldsymbol{\Theta}_i$ fixed and concentrate on optimizing P_{AP}. Consequently, we formulate the optimization problem for AP transmit power control [18], [19] as follows:

$$\max_{P_{AP}} \sum_{\forall k \in \mathcal{K}} \frac{P_{\mathrm{AP}}\beta_0 F(\psi_{i,0})\beta_k F(\psi_{i,k})\left|\mathbf{g}_{i,k}^H\boldsymbol{\Theta}_i\mathbf{h}_i\right|^2}{\sigma_k^2}, \quad (12a)$$
$$\text{s.t. (11b).}$$

It can be easily demonstrated that the optimization problem (12) is both affine and convex. This enables us to leverage the principles of convex optimization to find solutions. One approach involves differentiating the objective function with respect to P_{AP}, the transmit power of the AP. By equating this first-order derivative to zero while considering the constraint that limits the maximum transmit power, we can deduce the optimal solution as $P_{\mathrm{AP}} = \max\left\{0, P_{\mathrm{AP}}^{\max}\right\}$.

B. IRS Optimal Placement

In this subsection, we outline the subproblem in which the placement of the IRSs is optimized, with the IRS phase shift and radiation pattern held fixed, i.e., when $\boldsymbol{\Psi}_i$ and $\boldsymbol{\Theta}_i$ are known, and the optimal AP transmit power obtained from the previous sub-problem. Consequently, the optimization problem for determining each IRS central position can be formulated as follows:

$$\max_{\boldsymbol{s}^i[n]} \sum_{\forall k \in \mathcal{K}} \frac{c_0^2 F(\psi_{i,0})F(\psi_{i,k})\left|\mathbf{g}_{i,k}^H\boldsymbol{\Theta}_i\mathbf{h}_i\right|^2}{\sigma_k^2\|\boldsymbol{s}^i[n]-\boldsymbol{a}\|^{\alpha_0}\|\boldsymbol{s}^i[n]-\boldsymbol{u}[n,k]\|^{\alpha_k}}, \quad (13a)$$
$$\text{s.t. (11d).}$$

In this formulation, the $\boldsymbol{\beta}_i$'s are replaced by the IRSs' location decision variables, $\boldsymbol{s}^i[n]$. Notably, it is evident that the optimization problem (13) is convex in nature, facilitating the determination of an optimal solution. By equating the first-order derivative of the objective function with respect to $\boldsymbol{s}^i[n]$ to zero while taking into account the maximum SNR, we derive the quality shown on the top of the page, (14), for the each IRS central position in each 3D coordinates where it is assumed $\alpha_k = 2$ to achieve these closed-from solutions [16]. Now, an iterative approach can be employed to determine the optimal IRSs' position. Beginning with predefined or initial values for $s_x^i[n]$, $s_y^i[n]$, and $s_z^i[n]$, the optimal x-coordinate, y-coordinate and z-coordinate of the IRS are computed iteratively using (14) while adhering to constraint 11d. This iterative refinement process converges to optimize the IRS's placement within the 3D plane, driven by the system's performance metric and constraints.

Algorithm 1 Iterative AO Algorithm

Input: Set iteration number $e = 0$, maximum number of iterations $E_{\max}$, and and initialize the coordinates $P_{\mathrm{AP}} = P_{\mathrm{AP}}^0$, $\boldsymbol{\Psi}_e = \boldsymbol{\Psi}_e^0$, $\boldsymbol{\beta}_e = \boldsymbol{\beta}_i^0$, $\boldsymbol{\Theta}_e = \boldsymbol{\Theta}_e^0$.
    repeat
2:    Solve problem (11) for given $\{\boldsymbol{\Psi}_i^{e-1}, \boldsymbol{\beta}_i^{e-1}, \boldsymbol{\Theta}_i^{e-1}\}$ and obtain the optimal P_{AP}^e.
    Solve problem (12) for given $\{P_{\mathrm{AP}}^{e-1}, \boldsymbol{\Psi}_i^{e-1}, \boldsymbol{\Theta}_i^{e-1}\}$ and obtain the optimal $\boldsymbol{\beta}_i^e$.
4:    Solve problem (13) for given $\{P_{\mathrm{AP}}^{e-1}, \boldsymbol{\beta}_i^{e-1}\}$ and obtain the sub-optimal $\{\boldsymbol{\Psi}_i^e, \boldsymbol{\Theta}_i^e\}$.
    until e = $E_{\max}$
6: **return** $\{P_{\mathrm{AP}}^*, \boldsymbol{\Psi}_i^*, \boldsymbol{\beta}_i^*, \boldsymbol{\Theta}_i^*\} = \{P_{\mathrm{AP}}^e, \boldsymbol{\Psi}_i^e, \boldsymbol{\beta}_i^e, \boldsymbol{\Theta}_i^e\}$

C. Passive Beamforming and Radiation Pattern Optimization at the IRS

We now consider the subproblem of jointly optimizing $\boldsymbol{\Psi}_i$ and $\boldsymbol{\Theta}_i$ with fixed P_{AP} and $\boldsymbol{\beta}_i$, which can be given by:

$$\max_{\boldsymbol{\Psi}_i, \boldsymbol{\Theta}_i} \gamma_{i,k}(\boldsymbol{\Psi}_i, \boldsymbol{\Theta}_i), \quad (15a)$$
$$\text{s.t. (11c).} \quad (15b)$$

Unlike the previous two subproblems, which have closed-form solutions, finding closed-form solutions for $\boldsymbol{\Psi}_i$ and $\boldsymbol{\Theta}_i$ is a challenging task, primarily because of the constraints related to the unit modulus of the IRS elements. Fortunately, we can employ successive convex approximation methods to convert the rank unit modulus constraint into linear matrix inequalities in each iteration, as described in [20], [21] to find a sub-optimal solution. The Final iterative-based AO algorithm is provided in **Algorithm** 1.

IV. COMPLEXITY ANALYSIS

In this section, we delve into an analysis of the computational complexity of our proposed algorithm. Optimization problem (12) is a convex problem that can be efficiently solved in polynomial time. With only one optimization variable and a single convex constraint, its computational complexity per iteration is of the order $O_1 = \mathcal{O}(1)$. Optimization problem (13) is also convex but has $3IN$ decision variables and constrains, therefore, its complexity is $O_2 \approx \mathcal{O}((IN)^4))$. Finally, equation (15) can be reformulated into a Semi-Definite Program (SDP). The computational complexity for an SDP problem, with w SDP constraints, involving a positive semi-definite matrix of size $v \times v$, can be expressed as $O_3 = \mathcal{O}\left(\sqrt{v}\log(1/\zeta)(wv^3 + w^2v^2 + w^3)\right)$, where $\zeta > 0$ represents the solution accuracy, as detailed in [20]. Consequently, the overall complexity of the proposed solution is an order four polynomial $\mathcal{O}(e_{\mathrm{iter}}(O_2 + O_3))$, where e_{iter} is the number of iterations required for the AO approach to converge.

V. EVALUATION SETUP AND RESULTS

A. Evaluation Setup

One of the most relevant considerations when designing a virtual reality environment that intends to offer a fully-

$$\frac{\left(a_\triangle - s_\triangle^i[n]\right)}{(a_x - s_x^i[n])^2 + \left(a_y - s_y^i[n]\right)^2 + \left(a_z - s_z^i[n]\right)^2} = \frac{\left(s_\triangle^i[n] - u_\triangle[n,k]\right)}{(s_x^i[n] - u_y[n,k])^2 + \left(s_y^i[n] - u_y[n,k]\right)^2 + \left(s_z^i[n] - u_z[n,k]\right)^2},$$
$$\forall \triangle \in x, y, z, \ \forall k \in \mathcal{K}, \ \forall i \in \mathcal{I}, \ \forall n \in \mathcal{N}, \quad (14)$$

immersive experience is the precise tracking of the UE's spatial position and its subsequent three-dimensional imaging reconstruction. Accurate real-time tracking and representation of the UE's position enhances VR systems with more complex and realistic user interactions.

The scenarios in this section are based on finding the UE's 3D imaging reconstruction and location by combining mmWave Frequency Modulated Continuous Wave (FMCW) signals with IRS positioning. We base this work on the concept of an ISAC system assisted by an IRS to determine not only the capabilities of 3D representation but also the support to wireless communication trying to maximize both SNR and homogeneity in coverage throughout the UE.

As mentioned, we will be using FMCW signals in our setup. These types of signals exhibit a linear frequency change over time and can be mathematically described as:

$$m(t) = \cos\left(2\pi\left(f_c t + \frac{1}{2}Kt^2\right)\right), \quad 0 \leq t \leq T, \quad (16)$$

where f_c denotes the carrier frequency and $K = \frac{B}{T}$ represents the frequency slope. By leveraging the linear increase in frequency and the concept that time delay results in frequency shift, the Time of Flight (τ) can be estimated to then compute the distance to the target as $\tau = \frac{d_t(x,y,z)+d_{ri}(x,y,z)}{c}$. Taking into account the target reflectivity and round-trip decay, the received signal at the ith Receiver can be expressed as:

$$Sb_i(x, y, z, t) = \alpha_i e^{j2\pi \frac{K d_i(x,y,z)}{c} t}, \quad (17)$$

$$\alpha_i = \sigma_{0i} e^{j2\pi f_c \tau_i} \quad (18)$$

where α_i represents the attenuated amplitude from the ith Receiver in relation to the specified target, taking into account the distance and target reflectivity which in the evaluation setup is 0. It also contains the phase shift of the central frequency term.

As the objective is to reconstruct the user's 3D image, a single target or point reflector is insufficient. Therefore, the formulation needs to be expanded to account for multiple targets. The total received signal at the ith Receiver can be expressed as:

$$St_i(t) = \sum_{l=1}^{L} \alpha_{il} e^{j2\pi K \tau_{li} t} \quad (19)$$

where L represents the number of targets, that will depend on the the reflectivity of the points and their occlusion.

We assumed that the environment in which the VR system would be used is a square room with the IRS covering the walls, not including the floor or ceiling. It is a 3D environment in which the UE's and IRS's location and height relative to

TABLE I: Baseline simulations parameters

Parameter Name	Parameter Value
Transmit Power	10 mW
Rx Noise Figure	10 dB
Operating Frequency	77 GHz
Bandwidth	1.2 GHz
FMCW Sweep Time	0.8 ms
Sampling Rate	500 kHz
Number of IRS Elements	4000

the ground are taken into account. The size of the environment can have the dimensions of 10x10x3 m^2, 15x15x3 m^2, and 20x20x3 m^2, mimicking an apartment room, an office, or a conference room. Figure 1 depicts an example of this situation, which uses a random position of the IRS, User, and AP as an example.
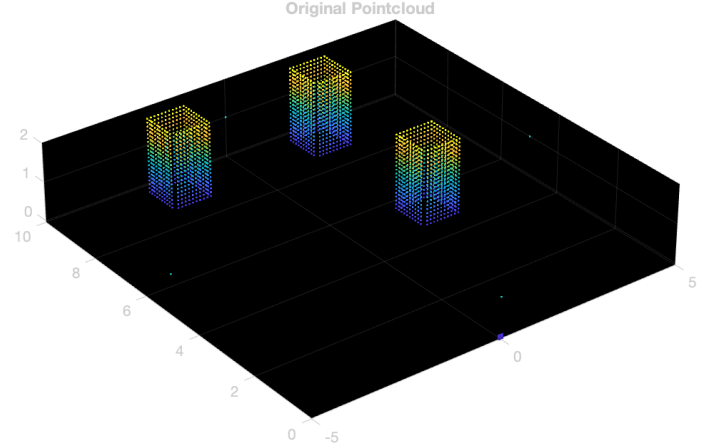

Figure 2: UE modeled as boxes in 10x10 with 3 users

To perform an exhaustive analysis and compare the homogeneity of the signal's SNR in different UE locations, we take into account an UE has 4 sides and can be modeled as a box (figure 2) and the simulation setup is equipped with 4 different algorithms. Firstly we have the *"NoIRS"* environment in which we only consider the signal from the AP. Secondly, a *"Random"* one, that places the center of the IRS at a random position along its corresponding wall. Additionally, we employ the *"Exhaustive Search"* algorithm, which seeks the optimal coordinates for the IRS. This exhaustive search involves examining all the walls of the room for each UE position, with the consideration of 1000 IRS placements for each wall. Thus, when dealing with 3 UEs, this algorithm will output the optimal locations for 12 IRS units, as each UE has one associated with each wall. Finally, the module has an *"Optimal"* algorithm explained in *IRS Optimal Placement*, which efficiently finds a sub-optimal solution significantly faster than the Exhaustive method.

This study involves an extensive simulation where a user undertakes a virtual trajectory spanning approximately 6 minutes within an enclosed environment. The scenarios encompass a user traversing a linear, predetermined virtual pathway or navigating a randomly generated virtual trajectory. The simulation is orchestrated across varying UE density scenarios, specifically incorporating configurations involving one, two, or three UEs who concurrently walk throw the designated virtual environment. As an example Figure 4 depicts the physical path of two U when they must follow a random course or a straight way in a virtual reality environment.
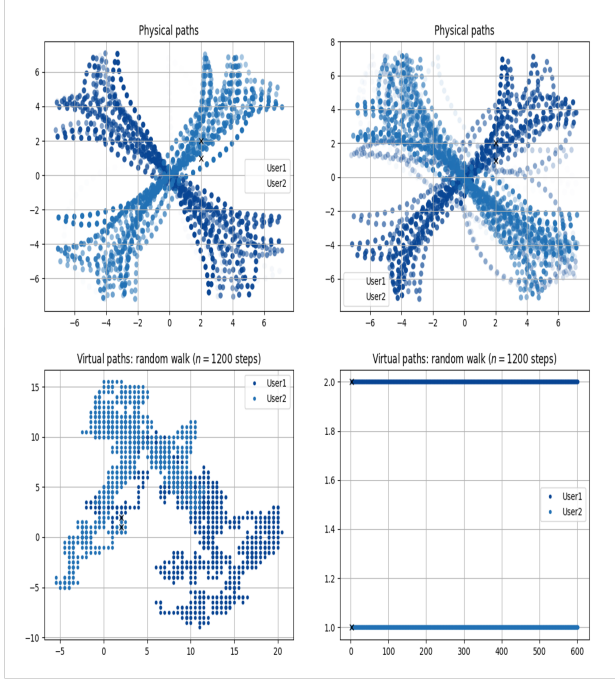

Figure 3: Physical and virtual path of two U when they follow a random or straight course in a VE

B. Evaluation Results

This exploration entails a comprehensive analysis that encapsulates a spectrum of connectivity scenarios with diverse room dimensions. We have measured the average Signal to Noise Ratio (SNR) and the standard deviation of this SNR (SD) in order to observe how performance in homogeneity increases in each scenario. These scenarios are conducted with the values of Table I, with 1, 2 and 3 users.

Table III presents the outcomes corresponding to the four specified scenarios in the evaluation setup, considering three different room sizes. The data for 1, 2, and 3 users are documented for each scenario. Each column, arranged from left to right, provides information on the Scenario, the number of users, the average Signal-to-Noise Ratio (SNR) for 1 user, the average SNR for all users, the average standard deviation of SNR, and the standard deviation of the averaged SNRs. It is noteworthy that the average SNR is computed by determining the SNR's Standard Deviation for the four sides of the User Equipment's (UE) box and subsequently averaging it. On the

other hand, the 'SD SNR' column directly calculates the standard deviation of the four average SNRs, each pertaining to a side of the UE's box.

The optimal placement of the Intelligent Reflecting Surface (IRS) significantly influences both the average standard deviation (SD) and the standard deviation of the averaged Signal-to-Noise Ratio (SNR) for each User Equipment (UE). In comparison to the 'NoIRS' and 'Random' scenarios, the exhaustive and optimal cases demonstrate substantially lower values for these metrics. For instance, in a 10x10 room, the Average SD ranges from 0.294 to 0.371 in the 'NoIRS' and 'Random' scenarios, while in the 'Exhaustive' scenario, it hovers around 0.2, and in the 'Optimal' scenario, it is approximately 0.25. A more pronounced contrast emerges when examining the SD of the Averaged SNR (SD SNR). In the 'NoIRS' and 'Random' scenarios, this value is approximately 0.7 and 0.25 (respectively), whereas in the 'Exhaustive' scenario, it ranges from 0.018 to 0.117, and in the 'Optimal' scenario, it's around 0.11. These results can be seen clearly in TABLE II, showing the SNR for each side of the wall in the 10x10 room with 1 user. It is important to remark that the positioning of the IRS for $Wall_x$ only takes into account the side of the user's box completely parallel to it.

TABLE II: UE's SNR coverage for each wall in 10x10

IRS	Wall 1	Wall 2	Wall 3	Wall 4	SD
No IRS	59,198	57,843	58,206	58,622	0,697
Random	58,206	58,442	57,957	58,79	0,2671
Exhaustive	56,501	56,487	56,527	56,684	0,091
Optimal	54,511	54,224	54,466	54,471	0,113

The optimization of homogeneity requires a loss in SNR. This decrease in SNR during exhaustive search and optimal placement is not uncommon and can be attributed to the granularity of the step used in IRS positioning. Occasionally, this granularity may lead to the selection of sub-optimal configurations. Additionally, to achieve homogeneity, the IRS positioning must adapt to the side with the smallest coverage, potentially sacrificing a potential SNR increase. Despite this, the decrease in SNR is needed in order to minimise the SD. The higher standard deviations in some scenarios imply increased fluctuations, potentially indicative of less reliable or consistent signal. Conversely, lower standard deviations signify more stability and consistency in the provided measurements across different room sizes.

Figure 4 illustrates the boxplots of Signal-to-Noise Ratio (SNR) values within the confines of a 20x20 room. The initial five boxplots correspond to the 'NoIRS' scenario, with the first one representing the averaged SNR for the four walls. Subsequently, the following four boxplots depict the SNRs for each wall of the User Equipment (UE). The subsequent five boxplots are associated with the 'Random' scenario, followed by those for the 'Exhaustive' scenario, and finally, for the 'Optimal' environment.

Observing the plots, it is evident that the variability in data for the first two scenarios is significantly larger, indicating less homogeneity and compactness. As previously noted, the SNR

is higher in these scenarios. In contrast, the 'Optimal' and 'Exhaustive' scenarios showcase lower variability, with data appearing more compact. Although the SNR is slightly lower in these cases compared to the former, the trade-off becomes apparent in the low variabilty of data. The 'Exhaustive' solution yields superior SNR and variability compared to the 'Optimal' one, albeit at the expense of a significantly longer runtime—approximately 15 times slower in practice (without employing data parallelization).

VI. Conclusion

References

[1] L. Muñoz-Saavedra *et al.*, "Augmented and virtual reality evolution and future tendency," *Applied sciences*, vol. 10, no. 1, p. 322, 2020.

[2] M. Chen *et al.*, "Virtual reality over wireless networks: Quality-of-service model and learning-based resource management," *IEEE Trans. Commun.*, vol. 66, no. 11, pp. 5621–5635, 2018.

[3] E. R. Bachmann *et al.*, "Multi-user redirected walking and resetting using artificial potential fields," *IEEE Trans. Vis. Comput. Graph.*, vol. 25, no. 5, pp. 2022–2031, 2019.

[4] F. Lemic *et al.*, "Predictive context-awareness for full-immersive multiuser virtual reality with redirected walking," *IEEE Commun. Mag.*, vol. 61, no. 9, pp. 32–38, 2023.

[5] J. Struye *et al.*, "CoVRage: Millimeter-wave beamforming for mobile interactive virtual reality," *IEEE Trans. Wirel. Commun.*, vol. 22, no. 7, pp. 4828–4842, 2023.

[6] D. Mehta *et al.*, "VNect: Real-time 3D human pose estimation with a single RGB camera," *ACM Trans. Graph.*, vol. 36, no. 4, pp. 1–14, 2017.

[7] Y. Wu *et al.*, "Sensing integrated DFT-spread OFDM waveform and deep learning-powered receiver design for terahertz integrated sensing and communication systems," *IEEE Trans. Commun.*, vol. 71, no. 1, pp. 595–610, 2022.

[8] P. Zhao *et al.*, "CubeLearn: end-to-end learning for human motion recognition from raw mmWave radar signals," *IEEE Internet Things J.*, vol. 10, no. 12, pp. 10 236–10 249, 2023.

[9] F. Lemic *et al.*, "Localization in power-constrained terahertz-operating software-defined metamaterials," *ELSEVIER Nano Commun. Netw.*, vol. 30, p. 100 365, 2021.

[10] S. Mohebi, M. Lecci, A. Zanella, and M. Zorzi, "The challenges of scheduling and resource allocation in ieee 802.11ad/ay," in *2020 Mediterranean Communication and Computer Networking Conference (MedComNet)*, 2020, pp. 1–4.

[11] P. Saxena and A. Kothari, "Performance analysis of adaptive beamforming algorithms for smart antennas," *IERI Procedia*, vol. 10, pp. 131–137, 2014.

[12] Q. Wu and R. Zhang, "Beamforming optimization for wireless network aided by intelligent reflecting surface with discrete phase shifts," *IEEE Transactions on Communications*, vol. 68, no. 3, pp. 1838–1851, 2020.

[13] W. Tang and t. y. v. n. p. others journal=IEEE Transactions on Wireless Communications,

[14] E. Björnson and L. Sanguinetti, "Power scaling laws and near-field behaviors of massive mimo and intelligent reflecting surfaces," *IEEE Open Journal of the Communications Society*, vol. 1, pp. 1306–1324, 2020.

[15] J. Jalali, A. Rezaei, A. Khalili, and J. Famaey, "Power-efficient joint resource allocation and decoding error probability for multiuser downlink miso with finite block length codes," in *2022 25th International Symposium on Wireless Personal Multimedia Communications (WPMC)*, 2022, pp. 232–237.

[16] J. Jalali and A. Khalili, "Optimal resource allocation for mc-noma in swipt-enabled networks," *IEEE Communications Letters*, vol. 24, no. 10, pp. 2250–2254, 2020.

[17] S. Bayat, J. Jalali, A. Khalili, M. R. Mili, S. Wittevrongel, and H. Steendam, "Optimal multi-objective resource allocation for d2d underlaying cellular networks in uplink communications," *IEEE Access*, vol. 9, pp. 114 153–114 166, 2021.

[18] J. Jalali *et al.*, "Power-efficient antenna switching and beamforming design for multi-user SWIPT with non-linear energy harvesting," in *2023 Proc. IEEE Consumer Commun. Netw. Conf. (CCNC)*, 2023, pp. 746–751.

[19] J. Jalali, A. Khalili, and H. Steendam, "Antenna selection and resource allocation in downlink miso ofdma femtocell networks," in *2020 IEEE 91st Vehicular Technology Conference (VTC2020-Spring)*, 2020, pp. 1–6.

[20] J. Jalali *et al.*, "Irs-based energy efficiency and admission control maximization for iot users with short packet lengths," *IEEE Transactions on Vehicular Technology*, pp. 1–6, 2023.

[21] J. Jalali *et al.*, "Is active IRS useful for mmwave wireless networks or not?" In *Proc. IEEE Int. Conf. Computing, Netw. Commun. (ICNC)*, 2023, pp. 377–382.

TABLE III: Coverage around UE

| IRS	U	10x10				15x15				20x20			
		SNRu	SNRt	Avg SD	SD SNR	SNRu	SNRt	Avg SD	SD SNR	SNRu	SNRt	Avg SD	SD SNR
No IRS	1	58,415	58,415	0,283	0,697	54,306	54,306	0,171	0,451	53,415	53,415	0,197	0,488
	2	58.438	58,623	0,287	0,717	54,306	55,088	0,171	0,451	53,697	53,514	0,197	0,488
		58,809		0,324	0,696	55,869		0,247	0,586	53,331		0,165	0,462
	3	58,438	58,587	0,287	0,717	54,306	54,741	0,178	0,451	53,697	53,202	0,197	0,488
		58,809		0,324	0,696	55,869		0,247	0,586	53,331		0,165	0,462
		58,515		0,294	0,675	54,048		0,165	0,441	51,537		0,148	0,373
Random	1	58,198	58,198	0,331	0,2671	54,571	54,571	0,201	0,649	51,998	51,998	0,135	0,656
	2	58,201	58,209	0,318	0,241	54,674	54,691	0,207	0,505	52,031	52,048	0,137	0,667
		58,218		0,344	0,341	54,707		0,214	0,267	52,067		0,131	0,801
	3	58,137	58,235	0,321	0,171	54,674	54,718	0,206	0,49	52,009	51,853	0,136	0,595
		58,401		0,371	0,309	54,826		0,233	0,384	52,012		0,129	0,693
		58,166		0,332	0,317	54,654		0,203	0,883	51,537		0,132	1,199
Exhaustive	1	56,505	56,505	0,206	0,091	52,688	52,688	0,138	0.211	49,859	49,859	0,102	0,1255
	2	56,564	56,492	0,197	0,0185	52,688	52,438	0,138	0,211	49,864	49,915	0,1102	0,125
		56,421		0,202	0,065	52,188		0,144	0,108	50,005		0,103	0,193
	3	56,564	56,503	0,197	0,021	52,688	52,515	0,131	0,211	49,825	49,922	0,102	0,125
		56,421		0,202	0,065	52,188		0,144	0,108	530,005		0,103	0,193
		56,525		0,213	0,117	52,668		0,132	0,036	49,935		0,094	0,117
Optimal	1	54,866	54,866	0,253	0,113	51,213	51,213	0,166	0,289	48,63	48,63	0,125	0,261
	2	55,534	55,049	0,244	0,118	51,772	51,409	0,165	0,241	48,803	48,781	0,124	0,266
		54,561		0,254	0,108	51,046		0,166	0,225	48,756		0,126	0,243
	3	55,534	55,049	0,244	0,118	51,772	51,251	0,165	0,241	48,803	48,717	0,124	0,266
		54,561		0,254	0,108	51,046		0,166	0,225	48,756		0,126	0,243
		55,341		0,263	0,195	51,061		0,163	0,276	48,592		0,124	0,301
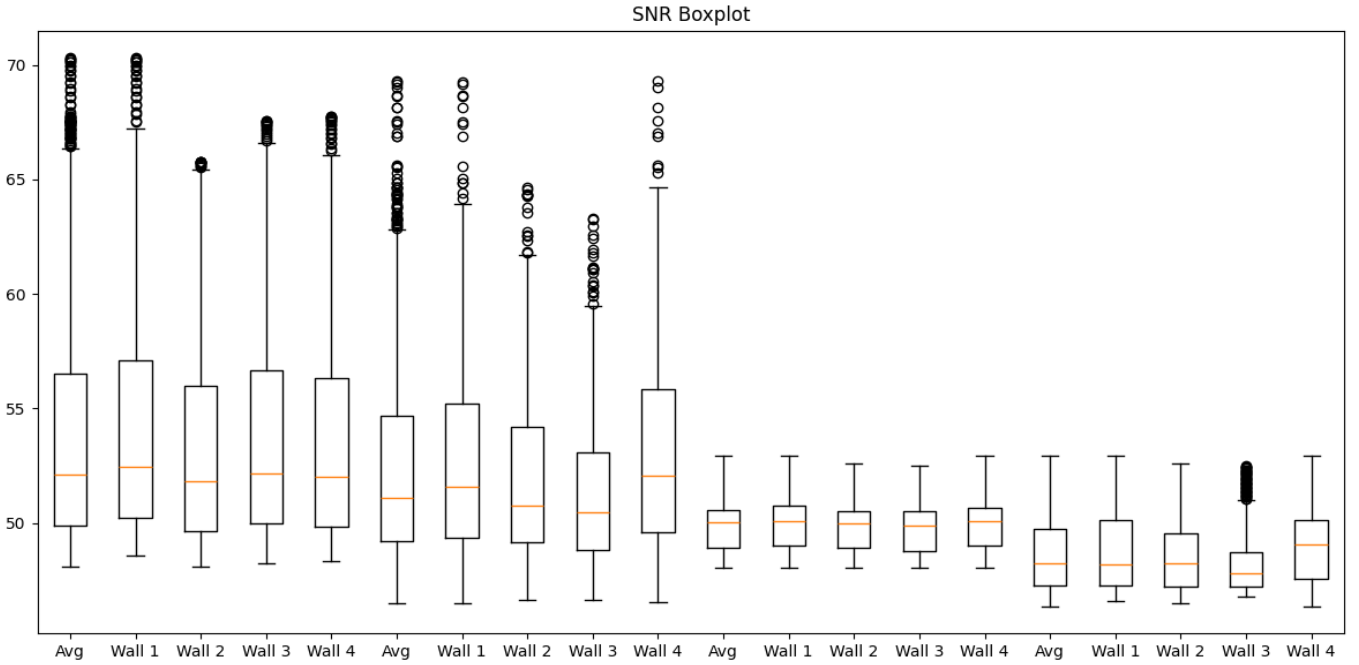
Figure 4: Boxplots of SNR in 20x20 room